Earth, Planets and Space

EXPRESS LETTER

Open Access

Magma migration beneath the active craters of Sakurajima volcano before the 2023 eruption of Showa crater inferred from ground deformation and muon monitoring

László Oláh[1,2*], Haruhisa Nakamichi[3], Takao Ohminato[4], Hiroyuki K. M. Tanaka[2,4] and Dezső Varga[1,2]

Abstract

Ground deformation source modeling and muographic mass density monitoring were applied for studying the plumbing system of Sakurajima volcano, Kyusu Japan using data collected by Interferometric Synthetic Aperture Radar and Sakurajima Muography Observatory. Lateral movement of ground deformation source was observed to east beneath the active craters around sea level that resulted in the shift of eruption frequency between the Minamidake craters. During the same period, muography showed opposite trends in mass changes for adjacent craters: mass decreased beneath the Minamidake A and B craters and mass increased beneath the Showa crater that also suggests the lateral movements of materials towards east. Thereafter, the ground deformation source started to rise and the eruption sequence of Showa crater started when the deformation source reached a depth of about 350–450 m beneath the craters. The muographically measured mass increased beneath Showa crater before the start of the eruption sequence. During eruption episodes of Minamidake A and B craters, the mass did not change beneath these craters and decreased beneath Showa crater, suggesting a connection between the adjacent craters. These observations suggest the presence of a deep magma channel around sea level which feeds Minamidake A and B craters and the existence of a shallow magma chamber about 350–450 m beneath the active craters which feeds all craters. Joint measurement of ground surface deformations and cosmic-ray muons allows simultaneous monitoring of shallow volcanic processes that may allow more reliable assessment of impending eruption sequences of Showa crater of Sakurajima volcano.

Keywords Muography, Cosmic-ray muon, InSAR, Ground deformation, Volcano, Magma, Conduit

*Correspondence:
László Oláh
olah.laszlo@wigner.hun-ren.hu
Full list of author information is available at the end of the article

Graphical Abstract

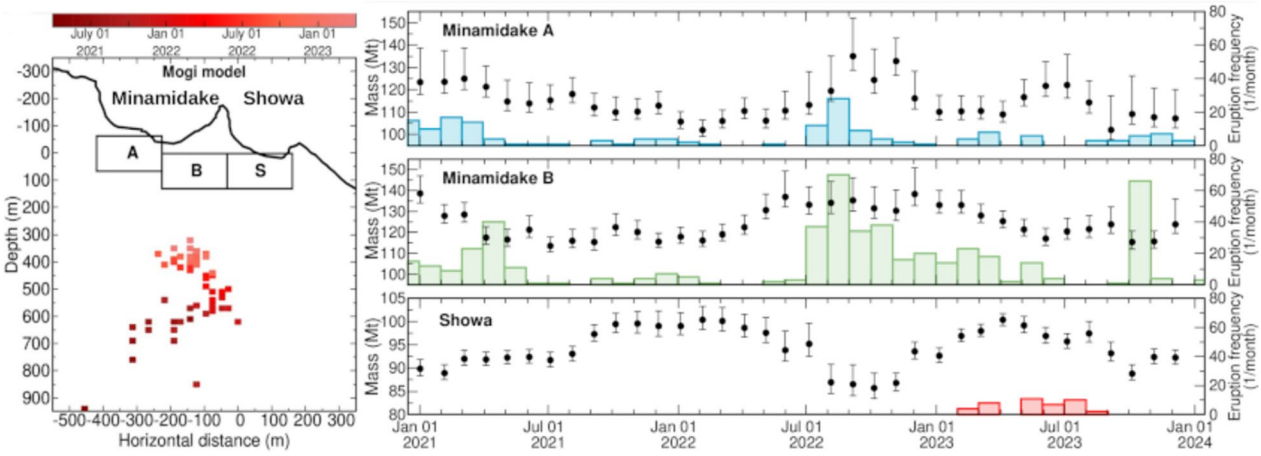

1 Introduction

Integration of complementary geophysical, geochemical, and petrological observations may allow us to explore the magma plumbing system, to study the volcanic processes that generate magma movements, and to elucidate how magma intrusion affects volcano deformation, eruption dynamics, etc. (Sparks et al. 2012; Magee et al. 2018). Monitoring the spatio-temporal evolution of magma has successfully been utilized for determining the spread of volcanic edifice (Donnadieu & Merle 2001; Donnadieu et al. 2001), localizing the onset of impending eruptions (D'Auria et al. 2012; Cannavò et al. 2015), and revealing the opening of new fissures (Pagli et al. 2012). These developments allowed the assessment of the occurrence of flank failures (Cervelli et al. 2006; Bonforte & Guglielmino 2015) and their possible secondary effects, such as tsunamis (Cervelli et al. 2002) or pyroclastic density currents (Belousov et al. 2020) that can affect even distant areas and result in more devastation.

Interferometric Synthetic Aperture Radar (InSAR) allows the detection of magma accumulation and tracking magma migration (Biggs et al. 2014). InSAR measures either pre-eruptive inflation of the ground surface due to magma intrusion (Patané et al. 2003) or syn-eruptive deflation of the volcanic edifice due to the release of volcanic ejecta (Massonnet et al. 1995). InSAR can be applied even at remote, inaccessible volcanic edifices. Modeling allows us to create a linkage between subsurface deformation sources and the measured surface deformation; it helps to interpret ground surface deformations and determine the position, volume, and pressure changes of magmatic ground deformation sources (e.g., Mogi 1958; McTigue 1987; Yang et al. 1988). Compiling global InSAR data sets and interpreting ground deformation and other monitoring data allowed us to reveal some limitations of InSAR: (A) about half of volcano deformations were followed by eruptive activities, and less than one-tenth of volcanoes erupted without precursory ground surface deformations (Biggs et al. 2014; Reath et al. 2019). (B) The ground surface deformations are indirect effects of subsurface phenomena, e.g., dormant craters can also uplift due to inflation sources located beneath the adjacent craters on multi-vent volcanoes (Oláh et al. 2023). (C) Elastic models cannot distinguish whether the effects on the intrusion are caused by pressure change or magma recharge (Fernández et al. 2001). (D) Modeling is sensitive to the presence of weak materials within the caldera (Masterlark 2007).

Applying density-sensitive complementary techniques, such as gravimetry (e.g., Fernández et al. 2001; Battaglia & Segall 2004; Poland & Anderson 2020) or muography (e.g., Tanaka 2019; Tanaka et al. 2023; Gibert et al. 2022; Macedonio et al. 2022), not only contributed to revealing the aforementioned limitations, but these may help to distinguish whether ground deformations are caused by either pressure changes or mass movements (Fernández et al. 2001; Oláh et al. 2023). Muography is based on the measurement of the yield of cosmic-ray muon particles. Muons are naturally occurring elementary particles created at 10–15 km altitude in Earth's atmosphere as the end product of particle physics processes induced by collisions of primary cosmic rays with the atmospheric nuclei. Muography allows remote, passive, and high-resolution scanning of the internal structure of large-sized structures, including volcanic edifices. The finite yield of muons (10,000 per square meter per minute at sea level)

is reduced by 3–4 orders of magnitude after penetrating rocks with a thickness of a few hundred of meters; thus, the applicability of muography is limited for the craters and upper conduits of volcanoes. Magmatic materials have already been imaged and monitored by muography. Tanaka et al. (2014) observed the uprise of magma in the conduit of Satsuma–Iwojima volcano during the 2013 eruption. Kusagaya & Tanaka (2015) revealed a dense region in Usu volcano that was interpreted as a past magma intrusion. Joint inversion of muographic and gravimetric data revealed an intruded magma body with a cylindrical shape in the Showa–Shinzan lava dome (Nishiyama et al. 2017). Multi-directional muography explored the highly welded vent of the scoria cone and three-directional radial dikes extending from the central vent in the Omuro-yama scoria cone (Nagahara et al. 2022). A magmatic body was visualized in the summit of Puy de Dôme volcano (Portal et al. 2013). We imaged plug formation (Oláh et al. 2019), explained a linkage between ground surface deformation and eruption frequency (Oláh et al. 2023), and explored the conduit structure (Oláh et al. 2024) in Sakurajima volcano, Japan.

Sakurajima volcano is supplied with magma from the Aira caldera located in northern Kagoshima Bay, and its southern peak is erupting from three craters, namely, Minamidake A, Minamidake B, and Showa. The type of eruptive activity is primarily Vulcanian (Gabellini et al. 2022). Eruption mechanism has been understood (Uhira & Takeo 1994; Iguchi 2013; Iguchi et al. 2013; Kazahaya et al. 2016). Different parts of the plumbing system have already been explored: continuous magnetotelluric observations revealed electrical resistivity changes due to movement of a mixture of magma and groundwater around the sea level (Aizawa et al. 2011). Absolute gravity measurements reconstructed the possible altitude of the magma head between 400 and 800 m altitudes above sea level (ASL) (Okubo et al. 2013). A dike intrusion event was also observed beneath the Showa crater between − 500 m and 300 m ASL by three-dimensional deformation mapping based on right- and left-loking ALOS2 InSAR (Morishita et al. 2016). Vent radius of Showa was estimated between 6.4 m and 42.3 m with a mean of 23.8 m from infrasound data (Muramatsu et al. 2018). The hypocenters of the earthquakes associated with explosive eruptions are estimated to be at the depth of 500 m beneath the bottom of the active craters by the seismic structure of the artificial seismic experiment (Nishimura et al. 2024). Muographically measured mass density changes allowed us to infer a branched connection between the Minamidake B and Showa craters (Oláh et al. 2024). In recent years, the eruptive frequency was observed to be typically a few tens of eruptions per month with a few dormant periods (Fig. 1a–c). Minamidake A and B craters erupted in recent years, and the Showa crater was active from 8 February to 4 August 2023. In this work, we analyze ground surface deformation and muon monitoring data to track the possible precursory magma migration before the eruption sequence of 2023 of Showa crater and infer the structure of the plumbing system.

2 Data collection and analysis methods

2.1 Experimental setting and data collection

Ground surface deformation of the volcanic edifice and the yield of cosmic-ray muons across the region of active craters were measured to observe simultaneously and interpret together both deep and shallow signals of volcanic activities. Our experimental setting is presented in Fig. 1d. Vertical displacements of the southern peak around the active craters were determined using the Phased Array type C-band Synthetic Aperture Radar images acquired by Sentinel-1 (The European Space Agency 2025) with a periodic time of 12 days (NEC 2025). NEC Corporation analyzed the InSAR images independently from this work and provided the vertical uplift data (Oláh et al. 2023, 2024). The vertical displacements were determined relative to the ground level measured on 6 April 2021 at 150 locations for the period from April 2021 to April 2023. Uncertainties of vertical uplifts measured by InSAR range between 0.005 m and 0.02 m in the crater region (e.g., Remy et al 2003). The yield of cosmic-ray muons was monitored across the southern peak of Sakurajima volcano with the multi-wire proportional chamber (MWPC)-based muography observation system (MMOS) of Sakurajima Muography Observatory (Oláh et al. 2019, 2023, 2024). The MMOS is a modular system that is operated with ten tracking system modules at a latitude of 31.557°N and a longitude of 130.650°E at 150 m

(See figure on next page.)

Fig. 1 **a, b, c** Eruption frequencies are shown on a monthly basis for the three active craters of Sakurajima volcano, namely, Minamidake A, Minamidake B and Showa. **d** Map of the measurement site is shown with the topography Sakurajima volcano (GSI 2024) and our experimental settings. Vertical uplifts were monitored by InSAR (ESA 2025) at the locations highlighted with red-colored dots. PQ line shows a slice that was selected across the crater region. O indicates the location of Sakurajima Muography Observatory at a latitude of 31.557° and a longitude of 130.650°. The black arrow indicates the orientation of muographic observation instruments. The inner map (Natural Earth 2025) shows the location of our experiment at Sakurajima volcano in Kagoshima Bay, Kyushu, Japan

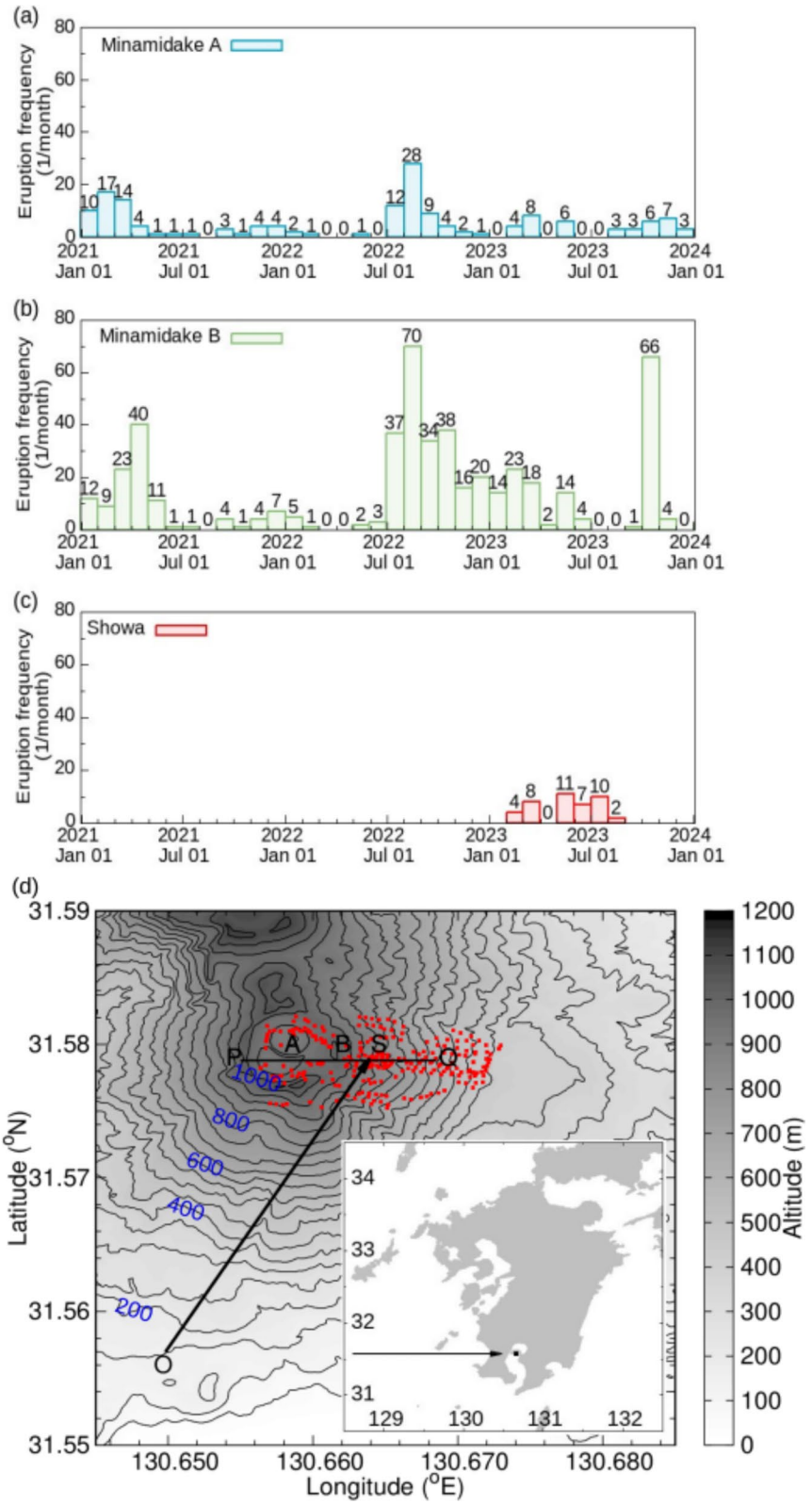

Fig. 1 (See legend on previous page.)

ASL at a distance of approx. 2,800 m from the active craters of Sakurajima volcano. The MMOS has already been presented extensively in Refs. (Oláh et al. 2018, 2021; Varga et al. 2020). We conducted data collection continuously between 1st October 2020 and 29th February 2024. Collection of muographic data has been stopped once per year when maintenance of MMOS was conducted.

2.2 Modeling of ground surface deformations

Ground surface deformations were localized near the peak region around the active craters, which hinted that the source of deformations may be located near the surface of the volcanic edifice. We localized the deformation source via quantifying the depth (D), the longitude, and the latitude coordinates by Mogi modeling (Mogi 1958; McTigue 1987) and Yang modeling (Yang et al. 1988) of vertical displacements (U_v). Figure 2a, andb, respectively, visualizes magma bodies as small spherical and ellipsoidal pressure sources of ground surface deformations. The spherical magma body has an r radius that is significantly smaller than its D depth. The surface displacement occurs in radial directions due to pressure change in the small spherical volume. The vertical component of ground surface deformation (U_v) at an R radial distance from the deformation source is expressed by the following equation:

$$U_{mod,v}(R) = 3\Delta V D/[4\pi(R^2 + D^2)^{3/2}] \quad (1)$$

For the ellipsoidal Yang source, the vertical component of ground deformation is expressed as follows:

$$U_{mod,v}(R) = \Delta P\, a\, b\, cD/[\mu(R^2 + D^2)^{3/2}] \quad (2)$$

where ΔP is the pressure change in the source, a, b, and c (a > b, a > c) are the three axes of the ellipsoid, and μ is the shear modulus of the surrounding medium.

Parameter estimation procedure based on grid searching via minimizing the square of relative difference

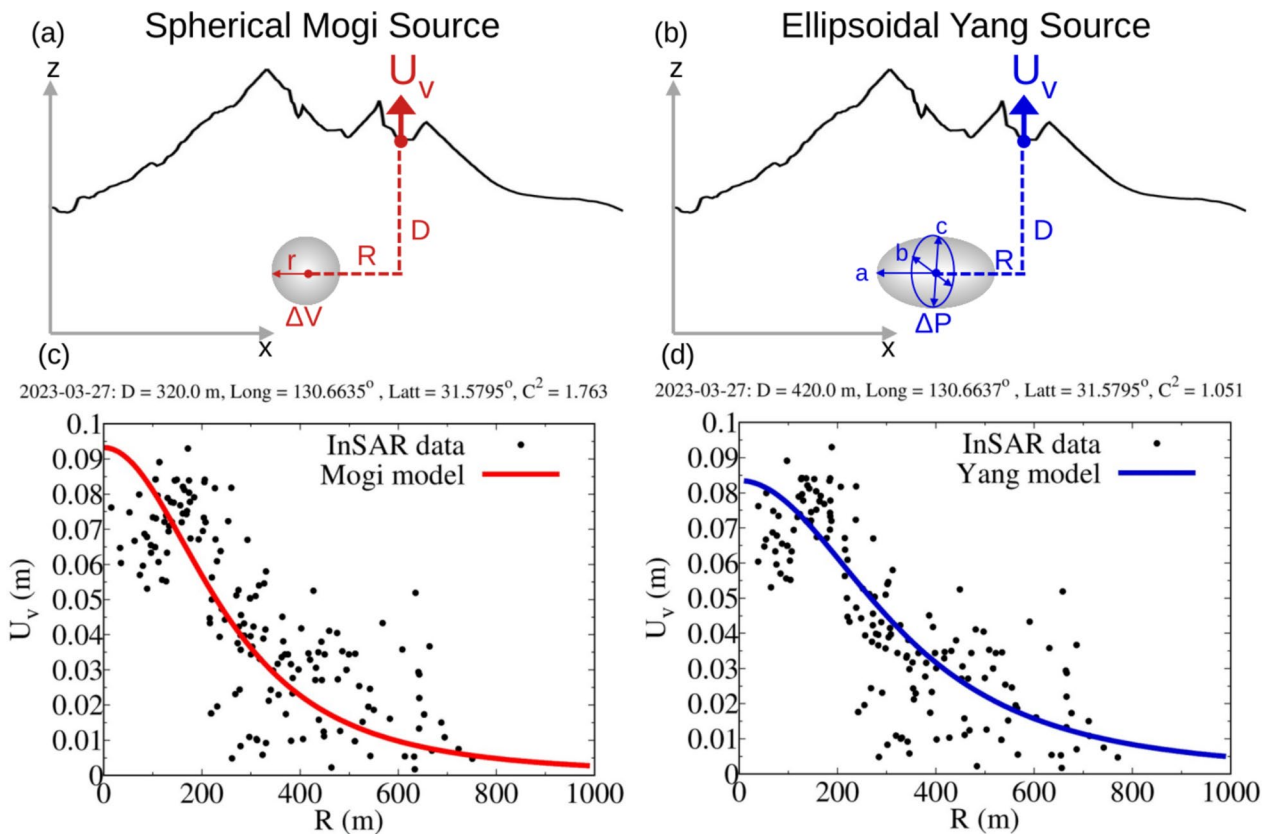

Fig. 2 **a** Schematic drawing of Mogi modeling shows a spherical pressure source with the radius r at depth D. The ΔV volume change of the Mogi source causes U_v vertical deformation on the surface of the volcanic edifice at an R radial distance. **b** Schematic drawing of Yang modeling shows an ellipsoidal pressure source with a,b, and c axes at depth D. The ΔP pressure change of the Yang source causes U_v vertical deformation on the volcano's surface at an R radial distance. **c, d** Vertical uplift is plotted as a function of radial distance from the deformation source. The red-colored line and the blue-colored line indicate the optimal U_v(R) curve for the Mogi model and Yang model, respectively. Black dots show the experimental vertical ground deformation data as a function of radial distance. Errors of U_v values range from 0.005 m to 0.02 m (e.g., Remy et al 2003)

between the measured and modeled vertical uplifts of ground surface (C^2) as a function of the radial distance of the measurement point from the deformation source:

$$C^2 = \sum_i \left[U_{meas,v}(R)_i - U_{mod,v}(R)_i\right]^2 / U_{mod,v}(R)_i^2 \tag{3}$$

where R was determined by the haversine formula from the latitude and longitude coordinates. The measured vertical uplift data were considered for altitudes above 700 m ASL. For optimization of the Mogi model, the ΔV volume change was set to be 40 Mm^3. For optimization of the Yang model, the pressure change was set to be 10 MPa and the shear modulus was set to be 6 GPa. All these fixed parameters were found by grid search with larger steps for other parameters. The a axis of the ellipsoid was varied from 200 to 300 m. The b and c axes of the ellipsoid were varied from 100 to 200 m. Step size was set to be 50 m for each axis. Other parameters were set to different values within the same ranges with the same steps for both models: the longitude and latitude coordinates were, respectively, varied in a range from 130.658° to 130.666° and from 31.579° to 31.581°. The step size was set to 0.00025° and 0.00050° for the longitude and the latitude, respectively. The depth from the crater floor was varied from 100 to 1000 m with a step size of 20 m. Figure 2c, d shows examples for comparison of vertical uplifts versus radial distance from source location for the experimental (black dots) data set and for the Mogi modeling (red-colored line) and for the Yang modeling (blue-colored line). Further data are presented in the supplementary materials. It is worth noting that the vertical uplifts varied within 2–3 mm at the same distances due to the deposition and removal of volcanic ejecta materials, which were not taken into account in the analysis of InSAR data. An F test (e.g., Gambino & Guglielmino 2008) was conducted to compare the two models. The F ratios were found to be below 1 for 55 of the 58 cases, which suggested that the Mogi model fits better onto the InSAR data. In this work, the errors of model parameters were derived from the grid size. We related the parameters of both models to the eruption frequencies and the muon monitoring data.

2.3 Muon data analysis and modeling

Event-by-event analysis procedure has been presented extensively in Ref. (Oláh et al. 2024). Here, we describe the analysis procedure in a nutshell. The procedure is initiated with reconstruction of clusters of muon hits on chamber by chamber. This reconstruction determined the cluster's centroids, sizes, and numbers. Thereafter, a combinatorial algorithm gathered the cluster centroids into track candidates and ordered them based on the goodness of line fit (chi-square per number of degrees of freedom, χ^2/ndf, where the ndf equals the number of detectors minus two), and selected the best-fitting track candidate with the smallest χ^2/ndf. In the last step, a track count histogram with a bin size of 0.023 in both directions was filled based on the horizontal and vertical slopes of tracks. After filling the track count histogram, flux was calculated for each angular bin by dividing the track counts by sensitive surface area, solid angle, and effective measurement time. Statistical flux error was determined by dividing the square root of track counts with the same quantities. Forward modeling of flux was conducted to determine the density across the volcanic edifice. The modeled flux was determined with different density lengths (density integrated over path length) by integrating the energy and elevation angle dependent spectra of muons (Tang et al. 2006) from threshold energies that are required for muons to penetrate the given density lengths (Groom et al. 2002). Path lengths were calculated using the digital elevation model of the edifice (Geospatial Information Authority of Japan 2024). The density value was extracted when the difference between the measured and modeled muon fluxes was found to be minimal. Figure 3 shows the densities for the measurement period with a bin size of 0.023 in both horizontal and vertical directions. This bin size corresponds to a spatial resolution of about 60 m beneath the active craters which located about 2800 m from the MMOS. The mass (m) was calculated for each region as follows:

$$\begin{aligned} m = & N\,\rho_{mean} T_{mean} [D^2\Delta^2 + (D + T_{mean})^2\Delta^2 \\ & + D\,(D + T_{mean})\,\Delta^2]/\,3 \end{aligned} \tag{4}$$

where N *is* the number pixels, ρ_{mean} is the aritmethic mean of density values within the selected region, and the following factors express the volume of a truncated rectangular pyramid, in which T_{mean} is the mean thickness of the selected region, D is the distance between the MMOS and the selected region that is 1820 m to the Minamidake A and Minamidake B craters and 1790 m to the Showa crater, and $\Delta = \Delta\tan(\theta_x) = \Delta\tan(\theta_y)$ is the slope bin size.

3 Results

3.1 Tracking magma migration by modeling ground deformation source

Figure 4 shows, respectively, the variations of the modeled parameters of the Mogi source (red-colored rectangles) and Yang source (blue-colored rectangles) from April 2021 to April 2023 and the eruption frequencies of active craters (colored boxes) from January 2021 to December 2023. The source kept its latitude within a range of 31.579°–31.581°, i.e., it moved neither north nor south throughout the measurement period from beneath

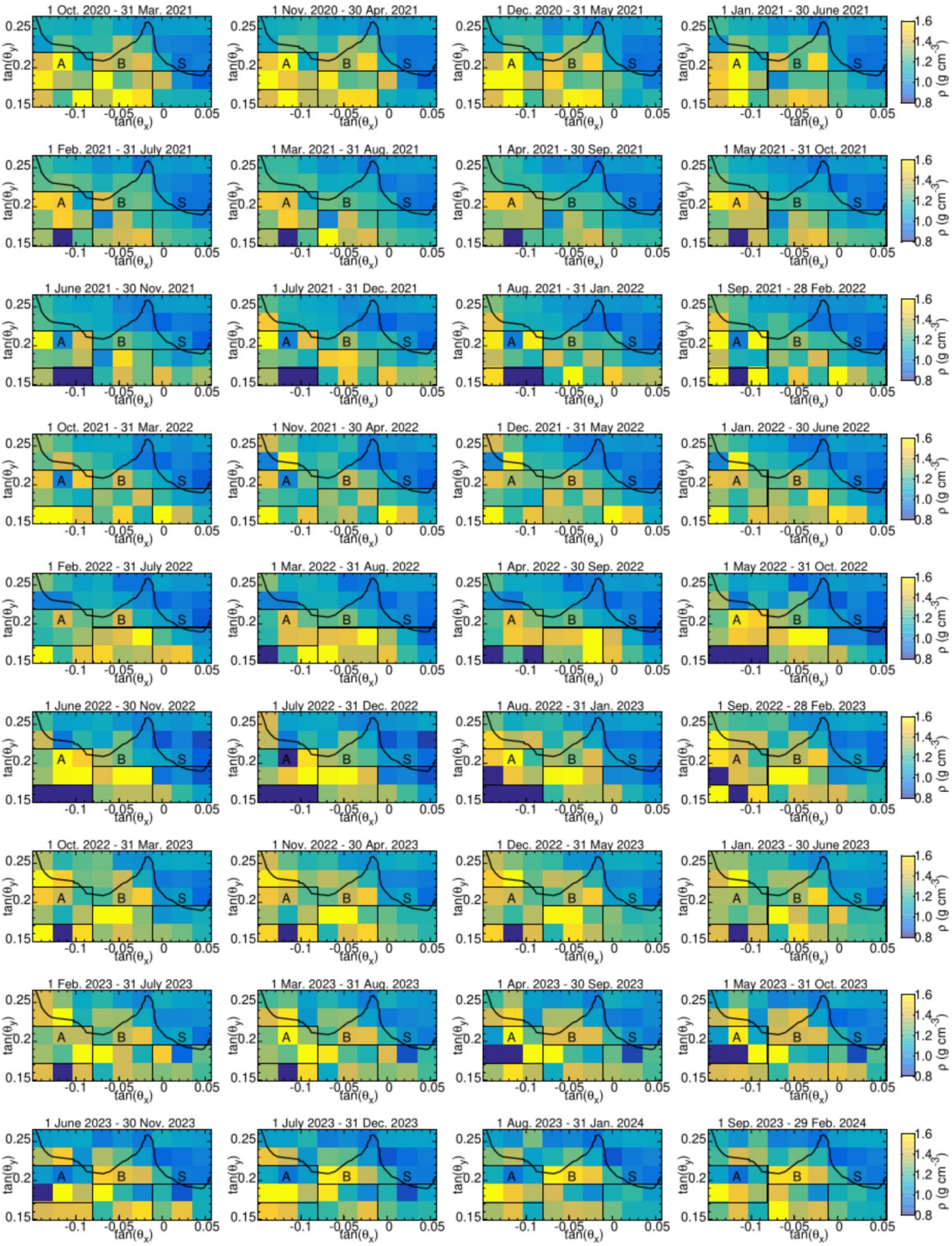

Fig. 3 Density images of the crater region of Sakurajima volcano are shown for a period from October 2020 to February 2024. Each image was produced using data collected throughout 6 months. A solid line indicates the cross section of volcanic edifice along the PQ line of Fig. 1d. Black rectangles designate the selected regions beneath the craters Minamidake A (A), Minamidake B (B) and Showa (S), respectively

the active craters (Fig. 4a). The variations of longitude coordinate indicate that the source of ground deformation shifted from the region located beneath Minamidake A crater to a region located beneath Minamidake B and Showa crater from April 2021 (Fig. 4b). This horizontal movement may resulted in the shift of eruptive activity from Minamidake A (blue-colored boxes) to Minamidake B (green-colored boxes). Throughout the entire measurement period, the deformation source rose from 900 m depth to 350–400 m depth relative to the level of Showa crater's floor (700 m ASL) (Fig. 4c). Since the latitude of the Mogi and Yang sources remained within a narrow range, we combined the longitudinal and the vertical variations of the deformation source in Fig. 4d, e. Here, the horizontal coordinates are shown relative to the observation axis (black arrow of Fig. 1d) of the muography observation instrument. The depth is measured relative to the floor of Showa crater. The shape of crater floors (black solid line) were extracted along the PQ line of Fig. 1d. Two phases are indicated for the movement of the deformation sources: (1) a rapid horizontal shift between the Minamidake A and Minamidake B occurred in 2021 and (2) a slower rising. The eruption sequence of Showa crater started (red-colored boxes in Fig. 4c) when the source reached the depth of about 350–400 m beneath the crater floor in February 2023.

3.2 Muon monitoring of shallow material transfers

We conducted offline analysis of muographic data (Oláh et al. 2024). The analysis procedures are presented in a nutshell in Methods section. In this work, we reconstructed the mass density images across the crater region and determined the total mass beneath the active craters. Figures 5a–c shows the 6-month average (arithmetic mean values) of masses with one standard deviation (black dots with error bars) for the regions beneath Minamidake A, Minamidake B, and Showa craters (black rectangles in Fig. 4d, e) and the monthly number of eruptions (colored boxes) from January 2021 to January 2024. Simultaneous changes were observed in the masses from January 2021 to March 2022: the total mass decreased beneath Minamidake A and Minamidake B by about 15–20 megatons (Mt) and increased beneath Showa by about 10 Mt. Throughout the same period, the eruptive activity shifted from Minamidake A (blue-colored boxes) to Minamidake B (green-colored boxes). The masses did not change beneath the craters during a relatively dormant period from March 2022 to May 2022. The masses increased beneath Minamidake A and B craters and decreased beneath Showa crater during the eruptive activities of the former two craters from May 2022 to October 2022. From November 2022 to May 2023, the mass started to decrease beneath Minamidake A and Minamidake B until the end of their eruption episodes, and the mass increased beneath Showa crater. Between May 2023 and August 2023, the mass decreased beneath Showa crater until the end of the eruption sequence. During the same period, the masses increased beneath the dormant Minamidake A and B craters. After the end of the eruption sequence in August 2023, the mass did not change beneath the Showa crater. Besides the crater regions, the average mass was monitored across a reference region in which volcanism did not occur, and the mass did not change here during the entire data collection period (Oláh et al. 2024).

4 Conclusions and discussion

Joint observation of Sakurajima volcano has been conducted with ground deformation and muon monitoring. Ground deformation source was modeled for tracking the shallow processes. Muography was conducted for monitoring the mass changes across the upper part of the volcanic edifice. The finite yield of muons allowed the imaging of the upper 120 m parts of conduits and craters of Sakurajima volcano during the measurement periods of 6 months. The mass sensitivity of muography allowed us to localize the ground deformation source more accurately than InSAR, e.g., in a previous work, the ground deformation data showed uplift in the region of Showa Crater, but it was caused by the magma located beneath Minamidake B crater (Oláh et al. 2023). Furthermore, muography helped to distinguish between the pressure change induced or mass intrusion induced ground deformations. Although muography could not pinpoint the source of ground deformation in these regions, the mass changes due to compressions and decompressions in

(See figure on next page.)

Fig. 4 Time evolution of the parameters of the ground deformation source was determined by Mogi modeling (red-colored rectangles) and Yang modeling (blue-colored rectangles) for the period from April 2021 to April 2023. **a** Longitude of ground deformation source versus time. **b** Latitude of ground deformation source versus time. Eruption frequencies of Minamidake A and B craters are, respectively, shown by blue-colored and green-colored boxes. **c** Variation of the depth of the deformation source from the floor of Showa crater over time. Eruption frequency of Showa crater is also shown by red-colored boxes. **d, e** Combination of panels (**b**) and (**c**) is shown. Black lines show the shape of Sakurajima volcano along the PQ line of Fig. 1d. Black rectangles indicate the regions of Minamidake craters A (A) and B (B), and Showa crater (S) that were monitored by muography

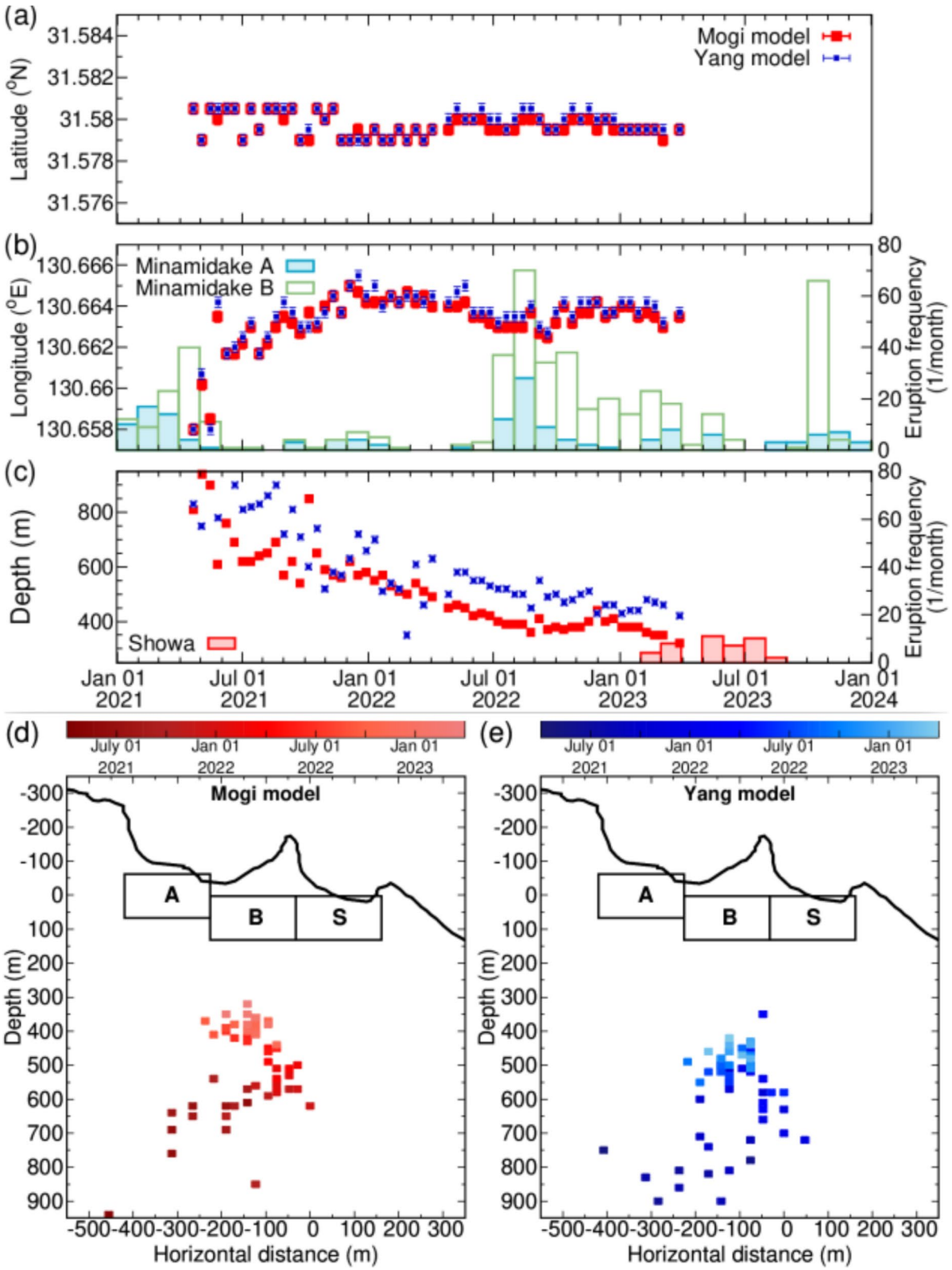

Fig. 4 (See legend on previous page.)

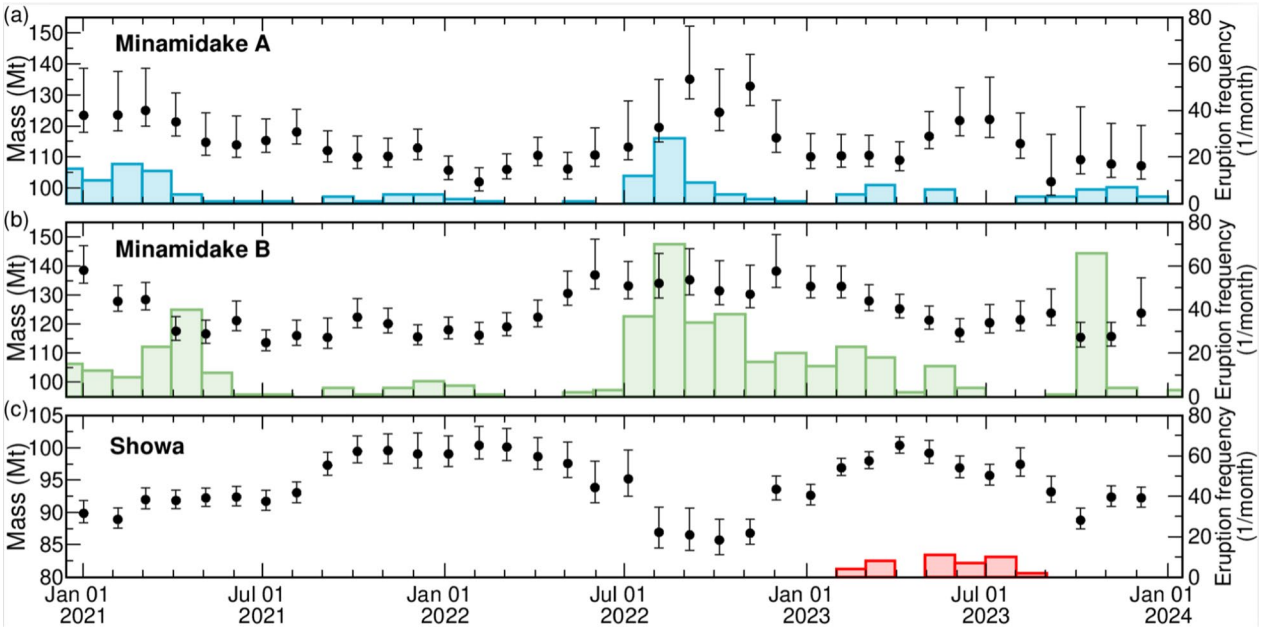

Fig. 5 Time series of total masses across the three active crater regions of Sakurajima volcano. The mass values (black dots) are shown with 1 standard deviation error bars from January 2021 to December 2023. The dots refer to the midpoints of time intervals. The colored boxes show the monthly number of eruptions for the Minamidake A (blue-colored boxes), Minamidake B (green-colored boxes) and Showa (red-colored boxes) craters. **a** Total masses are shown for the region beneath Minamidake A crater. **b** Total masses are shown for the region beneath the Minamidake B crater. **c** Total masses are shown for the region beneath the Showa crater

the mixture of gaseous and liquid materials beneath the volcanic plug could be quantified, and shallow volcanic processes could be studied more accurately. The observational results are discussed together for the following periods as follows.

From January 2021 to March 2022, a lateral movement of ground deformation source may occurred at a depth of 700–900 m beneath the floor of Showa crater. During the same period, the mass changes were, respectively, observed beneath the two Minamidake craters and the Showa crater to be minus 10 to minus 25 Mt and plus 10 Mt, which also indicates material transfer towards the Showa crater. Our interpretation is that the observed material transfers resulted in the shift of eruptive activities from Minamidake A (blue-colored boxes in Fig. 4b) to Minamidake B (green-colored boxes in Fig. 4b). The depth of lateral movement of the ground deformation source was found to be consistent with the depth of a fracture network reconstructed with magnetotelluric measurements conducted at 3.3 km east and 3 km west from Minamidake crater in 2008–2009 (Aizawa et al. 2011). The resistivity increased around sea level beneath the eastern measurement site in coincidence with the volcanic unrest. This resistivity increase was interpreted as a sign of lateral degassing of volatiles from a magma body. The results suggested the presence of a fracture network at a depth around sea level in which a mixture of groundwater and degassed volatiles can migrate laterally. Results of ground deformation source modeling also indicate a later path for magma that may support the presence of the fracture network.

During the eruption sequences of Minamidake B and Minamidake A craters occurred from May 2022 to October 2022; the masses increased by about 20 Mt beneath Minamidake A and B craters and decreased by about 15 Mt beneath Showa crater. These trends suggest material transfer from a shallow region beneath Showa crater to a shallow region beneath Minamidake craters. Magma intrusion may has caused the remaining mass increase.

During the period from November 2022 to May 2023, mass started to decrease beneath Minamidake A and Minamidake B until the end of their eruption episodes, and densities increased beneath Showa crater. Eruptive activities started in the Showa crater in February 2023 when the ground deformation source rose from a depth of 700–900 m to a depth of about 350–450 m beneath the bottom of the Showa crater. These observations suggest that the Showa crater activates when the magma reaches a sufficiently shallow depth beneath the active craters. This is similar to what was observed before earlier eruption episodes of Showa crater when the magma head was quantified between 400 and 800 m ASL by the absolute gravity measurements (Okubo et al. 2013). It is worth noting that the difference between the altitude of the current floor level and the earlier

reconstructed source altitude originates from the deepening and widening of the Showa crater (Japan Meteorological Agency 2018).

Between May 2023 and August 2023, the mass decreased by about 15 Mt beneath Showa crater until the end of the eruption sequence. We interpret this mass decrease as a decrease in magma feeding and release of volcanic ejecta. The former one resulted in the stop of eruptive activity. This is consistent with our earlier observations for the active Mindamidake craters (Oláh et al. 2023, 2024).

Observing a mass transfer between the active craters at shallow depth and activation of Showa crater as the ground deformation source reaches shallow depths of 350–450 m beneath the crater floor supports the presence of a common shallow magma storage and conduit system beneath the three craters. Seismic sources of explosive eruptions are located in and around a region at a depth of 400 m (Nishimura et al. 2024). Furthermore, geochemical analysis of samples from ejected rocks indicated that these rock samples are identical and originate from the same source (Matsumoto et al. 2013). A similar structure was observed at Mount Etna, in which short-term magma storage occurred close to the surface before a flank eruption and summit eruptive activity from a source located at a larger depth (Sanderson 1982).

We demonstrated that the joint analysis of ground deformation and muon data improves the reliability of the monitoring of the shallow parts of the volcano's plumbing system. Besides these data sets, we will analyze volcanic gas emission rates and earthquake data to provide a more robust assessment of impending eruption sequences of the active craters of Sakurajima volcano.

Abbreviations

ASL	Above sea level
InSAR	Interferometric synthetic aperture radar
MMOS	MWPC-based Muography Observation System
Mt	Megatons
MWPC	Multi-wire proportional chamber
ndf	Number of degrees of freedom

Supplementary Information

The online version contains supplementary material available at https://doi.org/10.1186/s40623-025-02325-3.

Supplementary Material 1.

Supplementary Material 2.

Supplementary Material 3.

Acknowledgements
The technical support provided by the members of the REGARD group is gratefully acknowledged. We would like to thank two anonymous reviewers and the editor Prof. Yuta Maeda for their helpful comments.

Author contributions
LO, TO, HKMT, and DV organized and conducted muon monitoring. LO conducted data analysis. LO, HN, and HKMT interpreted the data. LO wrote the text and prepared the figures. All authors read and approved the manuscript.

Funding
This work was supported by the Ministry of Education, Culture, Sports, Science and Technology, Japan (MEXT) Integrated Program for the Next Generation Volcano Research, the Joint Usage Research Project (JURP) of the University of Tokyo, Earthquake Research Institute, University of Tokyo (ERI) under project ID 2025-H-04, the Hungarian NKFIH research grant under identification number TKP2021-NKTA-10, the HUN-REN Welcome Home and Foreign Researcher Recruitment Programme KSZF-144/2023. Detector construction and testing was completed within the Vesztergombi Laboratory for High Energy Physics (VLAB) at HUN-REN Wigner RCP.

Data availability
The data sets generated during and/or analyzed during the current study are available from the corresponding author on reasonable request.

Declarations

Ethics approval and consent to participate
Not applicable.

Consent for publication
Not applicable.

Competing interests
All authors declare that they have no conflicts of interest.

Author details
[1]Institute for Particle and Nuclear Physics, HUN-REN Wigner Research Centre for Physics, Hungarian Research Network, 29-33 Konkoly-Thege Miklós Str, Budapest 1121, Hungary. [2]International Virtual Muography Institute (VMI), Tokyo, Japan. [3]Disaster Prevention Research Institute, Kyoto University, Gokasho, Uji, Kyoto 611-0011, Japan. [4]Earthquake Research Institute, The University of Tokyo, 1-1-1 Yayoi, Bunkyo, Tokyo 113-0032, Japan.

Received: 4 May 2025 Accepted: 7 November 2025
Published online: 24 December 2025

References

Aizawa K, Kanda W, Ogawa Y, Iguchi M, Yokoo A, Yakiwara H, Sugano T (2011) Temporal changes in electrical resistivity at Sakurajima volcano from observations. J Volcanol Geotherm Res 199:165–175. https://doi.org/10.1016/j.jvolgeores.2010.11.003

Battaglia M, Segall S (2004) The interpretation of gravity changes and crustal deformation in active volcanic areas. Pure Appl Geophys 161:1453–1467. https://doi.org/10.1007/s00024-004-2514-5

Belousov A, Belousova M, Hoblitt R, Patia H (2020) The 1951 eruption of Mount Lamington, Papua New Guinea: devastating directed blast triggered by small-scale edifice failure. J Volcanol Geotherm Res 401:106947. https://doi.org/10.1016/j.jvolgeores.2020.106947

Biggs J, Ebmeier SK, Aspinall WP, Lu Z, Pritchard ME, Sparks RSJ, Mather TA (2014) Global link between deformation and volcanic eruption quantified by satellite imagery. Nat Commun 5:3471. https://doi.org/10.1038/ncomms4471

Bonforte A, Guglielmino F (2015) Very shallow dyke intrusion and potential slope failure imaged by ground deformation: the 28 December 2014 eruption on Mount Etna. Geophys Res Lett 42:2727–2733. https://doi.org/10.1002/2015GL063462

Cannavò F, Camacho AG, González PJ, Mattia M, Puglisi G, Fernández J (2015) Real time tracking of magmatic intrusions by means of ground deformation modeling during volcanic crises. Sci Rep 5:10970. https://doi.org/10.1038/srep10970

Cervelli P, Segall P, Johnson K, Lisowski M, Miklius A (2002) Sudden aseismic fault slip on the south flank of Kilauea volcano. Nature 415:1014–1018. https://doi.org/10.1038/4151014a

Cervelli PF, Fournier T, Freymueller J, Power JA (2006) Ground deformation associated with the precursory unrest and early phases of the January 2006 eruption of Augustine Volcano, Alaska. Geophys Res Lett 33:L18304. https://doi.org/10.1029/2006GL027219

D'Auria L, Giudicepietro F, Martini M, Lanari R (2012) The 4D imaging of the source of ground deformation at Campi Flegrei caldera (southern Italy). J Geophys Res Solid Earth 117:8209. https://doi.org/10.1029/2012JB009181

Donnadieu F, Merle O (2001) Geometrical constraints of the 1980 Mount St. Helens intrusion from analogue models. Geophys Res Lett 28:639–642. https://doi.org/10.1029/2000GL011869

Donnadieu F, Merle O, Besson JC (2001) Volcanic edifice stability during cryptodome intrusion. Bull Volcanol 63:61–72. https://doi.org/10.1007/s004450000122

Natural Earth (2025) Free vector and raster map data. https://www.naturalearthdata.com/. Accessed 4 May 2025

Fernández J, Charco M, Tiampo KF, Jentzsch G, Rundle JB (2001) Joint interpretation of displacement and gravity data in volcanic areas. A test example: Long Valley Caldera, California. Geophys Res Lett 28(6):1063–1066. https://doi.org/10.1029/2000GL012393

Gabellini P, Cioni R, Geshi N, Pistolesi M, Miwa T, Lacanna G, Ripepe M (2022) Eruptive dynamics and fragmentation mechanisms during cyclic Vulcanian activity at Sakurajima volcano (Japan): insights from ash texture analysis. J Volcanol Geotherm Res 428:107582. https://doi.org/10.1016/j.jvolgeores.2022.107582

Gambino S, Guglielmino F (2008) Ground deformation induced by geothermal processes: a model for La Fossa Crater (Vulcano Island, Italy). J Geophys Res Solid Earth 113(B7):B07402. https://doi.org/10.1029/2007JB005016

Geospatial Information Authority of Japan (2024) GSI home page. http://www.gsi.go.jp/. Accessed 4 May 2025

Gibert D, de Bremond d'Ars J, Carlus B, Deroussi S, Ianigro J-C, Jessop DE, Jourde K, Kergosien B, Le Gonidec Y, Lesparre N, Marteau J, Moretti R, Nicollin F, Rosas-Carbajal M (2022) Observation of the dynamics of hydrothermal activity in La Soufrière of Guadeloupe volcano with joint muography, gravimetry, electrical resistivity tomography, seismic and temperature monitoring. Geophys Monogr Ser 270:55–73. https://doi.org/10.1002/9781119722748.ch5

Groom DE, Mokhov NV, Striganov SI (2002) Muon stopping power and range tables 10 MeV–100 TeV. At Data Nucl Data Tables 76:183–356. https://doi.org/10.1006/adnd.2001.0861

Iguchi M (2013) Magma movement from the deep to shallow Sakurajima Volcano as revealed by geophysical observations. Bull Volcanol Soc Japan 58:1–18. https://doi.org/10.18940/kazan.58.1_1

Iguchi M, Tameguri T, Ohta Y, Ueki S, Nakao S (2013) Characteristics of volcanic activity at Sakurajima Volcano's Showa Crater during the period 2006 to 2011. Bull Volcanol Soc Japan 58:115–135. https://doi.org/10.18940/kazan.58.1_115

Japan Meteorological Agency (2018) Report of 140th coordinating committee of prediction of volcanic eruption. https://www.data.jma.go.jp/svd/vois/data/tokyo/STOCK/kaisetsu/CCPVE/shiryo/140/140_01-3.pdf. Accessed 4 May 2025

Kazahaya R, Shinohara H, Mori T, Iguchi M, Yokoo A (2016) Pre-eruptive inflation caused by gas accumulation: insight from detailed gas flux variation at Sakurajima volcano, Japan. Geophys Res Lett 43:11219–11225. https://doi.org/10.1002/2016GL070727

Kusagaya T, Tanaka HKM (2015) Muographic imaging with a multi-layered telescope and its application to the study of the subsurface structure of a volcano. PJA-B 91:501–510. https://doi.org/10.2183/pjab.91.501

Macedonio G, Saracino G, Ambrosino F, Baccani G, Bonechi L, Bross A, Bongi M, Caputo A, Ciaranfi R, Cimmino L, Ciulli V, D'Alessandro R, D'Errico M, Giudicepietro F, Gonzi S, Masone V, Mori N, Noli P, Orazi M, Passeggio G, Peluso R, Pla-Dalmau A, Scarpato G, Strolin P, Vertechi E, Viliani L (2022) Muography of the volcanic structure of the summit of Vesuvius. Geophys Monogr Ser 270:123–136. https://doi.org/10.1002/9781119722748.ch9

Magee C, Stevenson CTE, Ebmeier SK, Keir D, Hammond JOS, Gottsmann JH, Whaler KA, Schofield N, Jackson CL-A, Petronis MS, O'Driscoll B, Morgan J, Cruden A, Vollgger SA, Dering G, Micklethwaite S, Jackson MD (2018) Magma plumbing systems: a geophysical perspective. J Petrol 59:1217–1251. https://doi.org/10.1093/petrology/egy064

Massonnet D, Briole P, Arnaud A (1995) Deflation of Mount Etna monitored by spaceborne radar interferometry. Nature 375:567–570. https://doi.org/10.1038/375567a0

Masterlark T (2007) Magma intrusion and deformation predictions: sensitivities to the Mogi assumptions. J Geophys Res Solid Earth 112(B6):B06419. https://doi.org/10.1029/2006JB004860

Matsumoto A, Nakagawa M, Amma-Miyasaka M, Iguchi M (2013) Temporal variations of the petrological features of the juvenile materials during 2006 to 2010 from Showa Crater, Sakurajima Volcano, Kyushu, Japan. Bull Volcanol Soc Japan 58:191–212. https://doi.org/10.18940/kazan.58.1_191

McTigue D (1987) Elastic stress and deformation near a finite spherical magma body: resolution of the point source paradox. J Geophys Res Solid Earth 92:12931–12940. https://doi.org/10.1029/JB092iB12p12931

Mogi K (1958) Relations between the eruption of various volcanoes and the deformation of the ground surface around them. Bull Earthquake Res Inst Univ Tokyo 36:99–134

Morishita Y, Kobayashi T, Yarai H (2016) Three-dimensional deformation mapping of a dike intrusion event in Sakurajima in 2015 by exploiting the right-and left-looking ALOS-2 InSAR. Geophys Res Lett 43:4197–4204. https://doi.org/10.1002/2016GL068293

Muramatsu D, Aizawa K, Yokoo A, Iguchi M, Tameguri T (2018) Estimation of vent radii from video recordings and infrasound data analysis: implications for Vulcanian eruptions from Sakurajima volcano, Japan. Geophys Res Lett 45:12829–12836. https://doi.org/10.1029/2018GL079898

Nagahara S, Miyamoto S, Morishima K, Nakano T, Koyama M, Suzuki Y (2022) Three-dimensional density tomography determined from multi-directional muography of the Omuroyama scoria cone, Higashi-Izu monogenetic volcano field, Japan. Bull Volcanol 84(10):94. https://doi.org/10.1007/s00445-022-01596-y

NEC (2025) Remote Sensing Solutions. https://www.nec.com/en/global/solutions/space/remote_sensing/index.html. Accessed 4 May 2025

Nishimura T, Kozono T, Matsumoto A, Nakagawa M, Iguchi M (2024) Vulcanian eruptions at Sakurajima Volcano: geophysical data, numerical modeling, and petrological evidence. Bull Volcanol 86:27. https://doi.org/10.1007/s00445-024-01722-y

Nishiyama R, Miyamoto S, Okubo S, Oshima H, Maekawa T (2017) 3D density modeling with gravity and muon-radiographic observations in Showa-Shinzan Lava Dome, Usu, Japan. Pure Appl Geophys 174:1061–1070. https://doi.org/10.1007/s00024-016-1430-9

Okubo S, Kazama T, Yamamoto K, Iguchi M, Tanaka Y, Sugano T, Imanishi Y, Sun W, Saka M, Watanabe A, Matsumoto S (2013) Absolute gravity variation at Sakurajima Volcano from April 2009 through January 2011 and its relevance to the eruptive activity of Showa Crater. Bull Volcanol Soc Japan 58:153–162. https://doi.org/10.18940/kazan.58.1_153

Oláh L, Tanaka HKM, Ohminato T, Varga D (2018) High-definition and low-noise muography of the Sakurajima volcano with gaseous tracking detectors. Sci Rep 8:3207. https://doi.org/10.1038/s41598-018-21423-9

Oláh L, Tanaka HKM, Ohminato T, Hamar G, Varga D (2019) Plug formation imaged beneath the active craters of Sakurajima volcano with muography. Geophys Res Lett 46:10417–10424. https://doi.org/10.1029/2019GL084784

Oláh L, Tanaka HKM, Hamar G (2021) Muographic monitoring of hydrogeomorphic changes induced by post-eruptive lahars and erosion of Sakurajima volcano. Sci Rep 11:17729. https://doi.org/10.1038/s41598-021-96947-8

Oláh L, Gallo G, Hamar G, Kamoshida O, Leone G, Llewellin EW, Lo Presti D, Nyitrai G, Ohminato T, Ohno S, Tanaka HKM, Varga D (2023) Muon imaging of volcanic conduit explains link between eruption frequency and ground deformation. Geophys Res Lett 50:e2022GL101170. https://doi.org/10.1029/2022GL101170

Oláh L, Hamar G, Ohminato T, Tanaka HKM, Varga D (2024) Branched conduit structure beneath the active craters of Sakurajima volcano inferred from muography. J Geophys Res Solid Earth 129:e2023JB028514. https://doi.org/10.1029/2023JB028514

Pagli C, Wright TJ, Ebinger CJ, Yun SH, Cann JR, Barnie T, Ayele A (2012) Shallow axial magma chamber at the slow-spreading Erta Ale Ridge. Nat Geosci 5:284–288. https://doi.org/10.1038/ngeo1414

Patané D, De Gori P, Chiarabba C, Bonaccorso A (2003) Magma ascent and the pressurization of Mount Etna's volcanic system. Science 299:2061–2063. https://doi.org/10.1126/science.1080653

Poland MP, Anderson KR (2020) Partly cloudy with a chance of lava flows: forecasting volcanic eruptions in the twenty-first century. J Geophys Res Solid Earth 125:e2018JB016974. https://doi.org/10.1029/2018jb016974
Portal A, Lazabuy P, Lénat J-F, Béné S, Boivin P, Busato E, Cârloganu C, Combaret C, Dupieux P, Fehr F, Gay P, Laktineh I, Miallier D, Mirabito L, Niess V, Vulpescu B (2013) Inner structure of the Puy de Dôme volcano: cross-comparison of geophysical models (ERT, gravimetry, muon imaging). Geosci Instrum Method Data Syst 2:47–54. https://doi.org/10.5194/gi-2-47-2013
Reath K, Pritchard M, Poland M, Delgado F, Carn S, Coppola D, Andrews B, Ebmeier SK, Rumpf E, Henderson S, Baker S, Lundgren P, Wright R, Biggs J, Lopez T, Wauthier C, Moruzzi S, Alcott A, Wessels R, Griswold J, Ogburn S, Loughlin S, Meyer F, Vaughan G, Bagnardi M (2019) Thermal, deformation, and degassing remote sensing time series (CE 2000–2017) at the 47 most active volcanoes in Latin America: implications for volcanic systems. J Geophys Res Solid Earth 124:195–218. https://doi.org/10.1029/2018JB016199
Remy D, Bonvalot S, Briole P, Murakami M (2003) Accurate measurements of tropospheric effects in volcanic areas from SAR interferometry data: application to Sakurajima volcano (Japan). Earth Planet Sci Lett 213:299–310. https://doi.org/10.1016/S0012-821X(03)00331-5
Sanderson T (1982) Direct gravimetric detection of magma movements at Mount Etna. Nature 297:487–490. https://doi.org/10.1038/297487a0
Sparks RSJ, Biggs J, Neuberg JW (2012) Monitoring volcanoes. Science 335:1310–1311. https://doi.org/10.1126/science.1219485
Tanaka HKM (2019) Japanese volcanoes visualized with muography. Philos Trans R Soc Lond A Math Phys Eng Sci 377(2137):20180142. https://doi.org/10.1098/rsta.2018.0142
Tanaka HKM, Kusagaya T, Shinohara H (2014) Radiographic visualization of magma dynamics in an erupting volcano. Nat Commun 5:3381. https://doi.org/10.1038/ncomms4381
Tanaka HKM, Bozza C, Bross A, Cantoni E, Catalano O, Cerretto G, Giammanco A, Gluyas J, Gnesi I, Holma M, Kin T, Lázaro Roche I, Leone G, Liu Z, Lo Presti D, Marteau J, Matsushima J, Oláh L, Polukhina N, Ramakrishna SSVS, Sellone M, Shinohara AH, Steigerwald S, Sumiya K, Thompson L, Tioukov V, Yokota Y, Varga D (2023) Muography. Nat Rev Methods Primers 3(1):88. https://doi.org/10.1038/s43586-023-00270-7
Tang A, Horton-Smith G, Kudryavtsev VA, Tonazzo A (2006) Muon simulations for Super-Kamiokande, KamLAND, and CHOOZ. Phys Rev D 74:053007. https://doi.org/10.1103/PhysRevD.74.053007
The European Space Agency (ESA) (2025) SAR instrument. https://sentinels.copernicus.eu/web/sentinel/home. Accessed 4 May 2025
Uhira K, Takeo M (1994) The source of explosive eruptions of Sakurajima volcano, Japan. J Geophys Res Solid Earth 99:17775–17789. https://doi.org/10.1029/94JB00990
Varga D, Nyitrai G, Hamar G, Galgóczi G, Oláh L, Tanaka HKM, Ohminato T (2020) Detector developments for high performance muography applications. NIMA 958:162236. https://doi.org/10.1016/j.nima.2019.05.077
Yang X-M, Davis PM, Dieterich JH (1988) Deformation from inflation of a dipping finite prolate spheroid in an elastic half-space as a model for volcanic stressing. J Geophys Res Solid Earth 93(B5):4249–4257. https://doi.org/10.1029/JB093iB05p04249

Publisher's Note